Modeling the lithospheric magnetic field over France by means of revised spherical cap harmonic analysis (R-SCHA)

E. Thébault,[1] M. Mandea,[1] and J. J. Schott[2]

Received 17 October 2005; revised 6 February 2006; accepted 16 February 2006; published 31 May 2006.

[1] We have recently proposed the revised spherical cap harmonic analysis (R-SCHA) modeling technique. The new mathematical functions represent faithfully the spatial variations of potential fields in a restricted area. In this paper, we tackle the inverse problem and outline the efficiency of the new basis functions with respect to real magnetic data. Processing simultaneously repeat stations, observatory, aeromagnetic, and CHAMP satellite data provides our first vector lithospheric field model over France, which extends from surface to 500 km of altitude. The magnetic field is represented with a minimum horizontal spatial representation of 40 km at the mean Earth radius. The magnetic lithospheric map consistency is confirmed with a comparison to known geological features. The model variation with altitude also suggests that the major French magnetic anomaly, the Paris basin anomaly, is produced by a deep-rooted geological structure. These results demonstrate the superiority of regional modeling over global modeling for delineating small-scale details in the lithospheric field. In view of forthcoming satellite missions, like Swarm, the revised spherical cap harmonic analysis method will help to accurately represent the lithospheric field for more detailed geological interpretations.

Citation: Thébault, E., M. Mandea, and J. J. Schott (2006), Modeling the lithospheric magnetic field over France by means of revised spherical cap harmonic analysis (R-SCHA), *J. Geophys. Res.*, *111*, B05102, doi:10.1029/2005JB004110.

1. Introduction

[2] The lithospheric magnetic field signal is mainly masked by the core field. A possible way to unravel the lithospheric field precisely is to combine information from both satellite and aeromagnetic measurements. The sparse distribution of ground data hampers the modeling of the lithospheric magnetic field at a high accuracy using the Spherical Harmonic representation. In order to circumvent this, all available data over a region of interest have to be considered and processed by means of a local mathematical scheme. In practice, several complementary data sets are available. Satellite data, measured at high altitudes, essentially detect the large magnetic field wavelengths and are sensitive to the deep magnetic structure buried in the crust. Aeromagnetic data recorded at low altitudes have higher resolutions and essentially detect the shallow magnetic bodies. When merging these data sets, with complementary spectral information content, we are likely to sample the complete magnetic lithosphere and to derive realistic high resolution lithospheric field models. These models can be used as a platform for geological studies and can help in delineating the geometry and depths of geological units. In practice, the solution is partly incomplete since data are inaccurate, smeared with errors and insufficient. For instance, intermediate wavelengths are neither well defined by satellite nor by aeromagnetic data [*Ravat et al.*, 2002], and a gap is unavoidable in the spectral representation of the magnetic field. Considering the better spectral coverage obtained by the configuration of the Swarm satellites, the situation will be considerably improved [*European Space Agency*, 2004]; thus we need to set up powerful mathematical tools to accurately represent the data at resolutions from kilometers to thousands of kilometers.

[3] Several regional modeling methods have been proposed in the past. Methods like polynomial modeling [*Le Mouël*, 1969] are suited for data measured at only one altitude but do not allow accurate downward or upward continuation of the field. The rectangular harmonic analysis (RHA), introduced by *Alldredge* [1981], implies a flat Earth approximation and is less accurate as the altitude increases [*Langel and Hinze*, 1998, section 5.3]. The spherical cap harmonic analysis (SCHA), proposed by Haines, was developed to obtain models of the lithosphere in large regions [*Haines*, 1985]. This latter method also deals inadequately with data recorded at different altitudes and models become unrealistic when considering aeromagnetic and satellite data together. The errors incurred in each of these modeling techniques are difficult to estimate exactly. Thus, considering that current satellite sensitivities detect very weak magnetic signals, like tidal [*Tyler et al.*, 2003] or ocean induction effects [*Manoj et al.*, 2006], we cannot consent to apply approximate mathematical tools.

[1] GeoForschungsZentrum, Potsdam, Germany.
[2] Ecole et Observatoire des Sciences de la Terre, Strasbourg, France.

0148-0227/06/2005JB004110$09.00

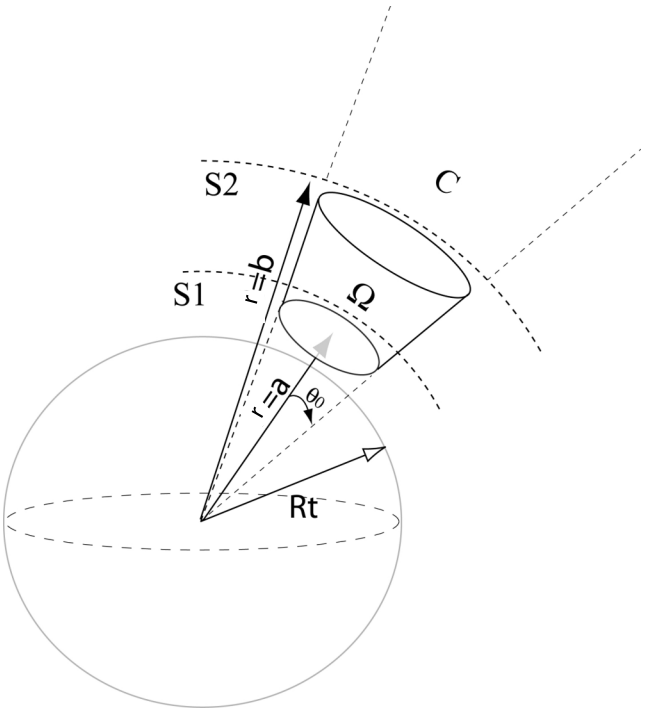

Figure 1. Magnetic field represented within a closed region resulting from the intersection of two spheres (S1 and S2) of radii a and b, with an infinite cone (C) of half aperture θ_0.

[4] The revised spherical cap harmonic analysis (R-SCHA) is a modeling technique designed to be applied at a regional scale [*Thébault et al.*, 2006]. In the ideal case of infinite series expansion, there is no approximation. As a result, the information concealed in data measured at different altitudes, from ground to satellite levels, can now be retained by the modeling. In this paper we explore the feasibility and the consistency of this method and apply R-SCHA to a combination of different magnetic data sets. For the present application, we choose the French metropolitan territory. The method could be applied to any region well covered by different and complementary data sets. We chose to focus on the French region for two reasons; first, a large amount of aeromagnetic and satellite data, both of good quality, are available, and the French total field anomaly map derived by *Le Mouël* [1969] shows good correlations with geological evidences. This gives us a chance to compare objectively our results obtained by R-SCHA with a previous study. Secondly, a new interest for this region has recently been revived [*Truffert et al.*, 2001] and some processes responsible for magnetic anomalies remain enigmatic [*Pham et al.*, 2000]. In this context, we considered it poignant to produce vector maps for the lithospheric magnetic anomalies derived from the most recent CHAMP satellite data, aeromagnetic surveys, repeat stations and observatory data. The main aim of this paper is to apply this new modeling technique to a real data situation and to provide some geological discussion. We hope that the new maps, having a minimum spatial wavelength of 40 km, will bring information to a new level and help improve the reconstruction of France's geological past.

2. Theoretical Background

[5] In a source free region such as Ω, delimited by minimal and maximal radial distances $r = a$ and $r = b$ and a cone C with half angle θ_0 (Figure 1), the magnetic field may be expressed by means of basis functions solving the Laplace equation $\nabla^2 V = 0$.

[6] In order to form a complete boundary value problem (BVP), the Laplace equation may be associated with boundary conditions on the surfaces of Ω such that

$$\nabla^2 V = 0 \tag{1a}$$

$$V|_{\theta=\theta_0} = F(r,\varphi) \tag{1b}$$

$$\left.\frac{\partial V}{\partial r}\right|_{r=a} = -G_a(\theta,\varphi) \tag{1c}$$

$$\left.\frac{\partial V}{\partial r}\right|_{r=b} = G_b(\theta,\varphi) \tag{1d}$$

The solution of this BVP is obtained by splitting it into two subproblems [*Thébault et al.*, 2004]. The independent solution of the subproblems leads to the construction of a complete basis function for the potential inside the region of interest. The overall solution for the potential is [*Thébault et al.*, 2006]

$$\begin{aligned} V(r,\theta,\varphi) = {} & a\sum_{k\geq 1}\sum_{m\geq 0}\left(\frac{a}{r}\right)^{n_k+1}\left(G^{i,m}_{n_k}\cos(m\varphi)+H^{i,m}_{n_k}\sin(m\varphi)\right) \\ & \cdot P^m_{n_k}(\theta) + a\sum_{k\geq 1}\sum_{m\geq 0}\left(\frac{r}{a}\right)^{n_k}\left(G^{e,m}_{n_k}\cos(m\varphi)+H^{e,m}_{n_k}\sin(m\varphi)\right) \\ & \cdot P^m_{n_k}(\theta) + a\sum_{p\geq 0}\sum_{m\geq 0}R_p(r)\left(G^m_p\cos(m\varphi)+H^m_p\sin(m\varphi)\right)K^m_p(\theta) \end{aligned} \tag{2}$$

with $P^m_{n_k}$ the associated Schmidt seminormalized Legendre functions of integer order m, generally real degrees n_k, and $K^m_p(\theta)$ the conical or Mehler functions [*Thébault et al.*, 2006]. Henceforth, we refer to the functions involving $K^m_p(\theta)$ as the Mehler or the conical functions; the corresponding coefficients are named the Mehler coefficients. In contrast, the basis function related to $P^m_{n_k}$ functions are named the Legendre functions; the corresponding coefficients are named the Legendre coefficients. $R_p(r)$ are radial functions, comparable to Fourier series. They depend on the integral index p and the lower and upper radii a and b such that

$$R_0 = \text{const} \tag{3}$$

$$\begin{aligned} R_p(r) = A\sqrt{\frac{a}{r}}\Bigg[& \frac{2\pi p}{\log\left(\frac{b}{a}\right)}\cos\left(p\pi\frac{\log\left(\frac{r}{a}\right)}{\log\left(\frac{b}{a}\right)}\right) \\ & + \sin\left(p\pi\frac{\log\left(\frac{r}{a}\right)}{\log\left(\frac{b}{a}\right)}\right)\Bigg] \quad p>0 \end{aligned} \tag{4}$$

with A a constant depending on the normalization adopted. It directly follows that the magnetic field, represented by the negative gradient of the potential $\mathbf{B}(\mathbf{r}, \theta, \varphi) = -\nabla V$, writes

$$X = \frac{a}{r}\sum_{m=0}^{\infty}\sum_{p=0}^{\infty} R_p(r)\frac{dK_p^m}{d\theta}\left\{G_p^m\cos(m\varphi) + H_p^m\sin(m\varphi)\right\} + \sum_{m=0}^{\infty}\sum_{k=0}^{\infty}\left(\frac{a}{r}\right)^{n_k+2}\frac{dP_{n_k}^m}{d\theta}\left\{G_{n_k}^{m,i}\cos(m\varphi) + H_{n_k}^{m,i}\sin(m\varphi)\right\} + \sum_{m=0}^{\infty}\sum_{k=0}^{\infty}\left(\frac{r}{a}\right)^{n_k-1}\frac{dP_{n_k}^m}{d\theta}\left\{G_{n_k}^{m,e}\cos(m\varphi) + H_{n_k}^{m,e}\sin(m\varphi)\right\} \quad (5)$$

$$Y = \frac{a}{r}\sum_{m=1}^{\infty}\sum_{p=0}^{\infty} R_p(r)\frac{mK_p^m}{\sin\theta}\left\{G_p^m\sin(m\varphi) - H_p^m\cos(m\varphi)\right\} + \sum_{m=1}^{\infty}\sum_{k=0}^{\infty}\left(\frac{a}{r}\right)^{n_k+2}\frac{mP_{n_k}^m}{\sin\theta}\left\{G_{n_k}^{m,i}\sin(m\varphi) - H_{n_k}^{m,i}\cos(m\varphi)\right\} + \sum_{m=1}^{\infty}\sum_{k=0}^{\infty}\left(\frac{r}{a}\right)^{n_k-1}\frac{mP_{n_k}^m}{\sin\theta}\left\{G_{n_k}^{m,e}\sin(m\varphi) - H_{n_k}^{m,e}\cos(m\varphi)\right\} \quad (6)$$

$$Z = \sum_{m=0}^{\infty}\sum_{p=0}^{\infty}\frac{dR_p(r)}{dr}K_p^m\left\{G_p^m\cos(m\varphi) + H_p^m\sin(m\varphi)\right\} - \sum_{m=0}^{\infty}\sum_{k=0}^{\infty}(n_k+1)\left(\frac{a}{r}\right)^{n_k+2}P_{n_k}^m\left\{G_{n_k}^{m,i}\cos(m\varphi) + H_{n_k}^{m,i}\sin(m\varphi)\right\} + \sum_{m=0}^{\infty}\sum_{k=0}^{\infty}n_k\left(\frac{r}{a}\right)^{n_k-1}P_{n_k}^m\left\{G_{n_k}^{m,e}\cos(m\varphi) + H_{n_k}^{m,e}\sin(m\varphi)\right\} \quad (7)$$

and the total intensity F is defined by

$$F = \sqrt{(X^2 + Y^2 + Z^2)} \quad (8)$$

with X, Y, and Z, the north, east and downward component of the magnetic field $\mathbf{B}$. The coordinates θ and φ are the colatitude and the longitude, respectively, in the cone reference frame. As already stressed, the method is exact in the limit of infinite series expansions. In practice, the number of available data, their distribution, and the rate of convergence of the local functions, may hamper the accurate modeling of the total field. A regional modeling technique like R-SCHA is more efficient when dealing with a residual field because the errors incurred in truncating the series is less prominent [*Thébault et al.*, 2006]. For this reason, we consider only the representation of the residual field, which will result from the difference between the magnetic measurements, $\mathbf{B_m}$ or F_m, and a core field model, $\mathbf{B_c}$ or F_c, such that

$$\delta B(r, \boldsymbol{\theta}, \boldsymbol{\varphi}) = \mathbf{B}_m(r, \boldsymbol{\theta}, \boldsymbol{\varphi}, t) - \mathbf{B}_c(r, \boldsymbol{\theta}, \boldsymbol{\varphi}, t) \quad (9)$$

and the anomaly intensity

$$\delta F(r, \boldsymbol{\theta}, \boldsymbol{\varphi}) = F_m(r, \boldsymbol{\theta}, \boldsymbol{\varphi}, t) - F_c(r, \boldsymbol{\theta}, \boldsymbol{\varphi}, t) \quad (10)$$

[7] We assume here that the data are reduced for the external field. Our purpose is to coestimate the most appropriate set of parameters, or pseudo-Gauss coefficients $\{G_p^m, H_p^m\}$, $\{G_{n_k}^{m,i}, H_{n_k}^{m,i}\}$, $\{G_{n_k}^{m,e}, H_{n_k}^{m,e}\}$, that represent the field over France, from ground to satellite altitudes. The superscripts 'i' and 'e' refer to internal and external according to the shape of the radial basis function a/r or r/a involved. So far, we cannot assign a particular meaning to each of these pseudo-Gauss coefficients. A limitation of the R-SCHA approach is that it is difficult to separate the internal from the external field just by studying the Gauss coefficients $G_{n_k}^{m,i}$ or $G_{n_k}^{m,e}$. Modeling the lithospheric field therefore requires a preprocessing, which cleans the data from the unwanted magnetic field contributions [*Thébault et al.*, 2006].

3. Data Sets and Data Processing

[8] We consider the independent data recorded at different epochs and altitudes over France where aeromagnetic data, repeat stations data and satellite data are available. The geometry of the truncated cone is defined according to data distribution. In order to improve the conditioning of the inverse problem, it is necessary to define its boundaries so that the data are distributed as evenly as possible within the domain. The cone is centered on the geocentric latitude $\Theta = 46.5°$ and longitude $\Phi = 1.3°$. The half angle of the cone, set to $\theta_0 = 5°$, is chosen such that the aeromagnetic data optimally cover the lowest surface. Lower and upper boundaries are defined according to the minimum and the maximum altitudes contained in the entire data set. The upper radius b is defined by $b = R_t + E_{\max}$ according to the highest satellite orbit, with $R_t = 6371.2$ km, the Earth reference radius. Considering the maximum CHAMP satellite orbit over France, we define $E_{\max} = 500$ km. Similarly, the lowest altitude $E_{\min}$ contained in the data allows us to set $a = R_t + E_{\min}$. Note that a is not necessarily the Earth's mean radius in R-SCHA modeling. Considering the repeat stations altitudes, measured in a geodetic reference frame, we may have $a < R_t$ in the geocentric reference frame (see section 3.1). This negative value simply means that the ellipsoid is lower than the mean Earth's radius in the region under study. It is worth reminding that as soon as the geometric parameters are established, the local set of pseudo-Gauss coefficients make sense only for a given set of parameters $\{\Theta, \Phi, \theta_0, E_{\min}, E_{\max}\}$ that must remain unchanged.

3.1. Repeat Stations Data and Observatory Data

[9] In 1965, the French repeat network was improved by adding 19 stations to the 12 existing ones and by using a proton magnetometer for total field measurements. Other existing data before 1965 are not considered in the present study. From 1965 onward, the French repeat stations network comprises 29 metropolitan points located 150–200 km apart (Figure 2). During the five decades of measurements, the locations were preserved except for a few repeat stations. These displacements, listed in the Bureau Central de Magnétisme Terrestre publications (BCMT [*Mandea*, 2001]), were taken into account during the different stages of the processing.

[10] The Chambon-La-Forêt observatory annual means and the repeat stations data are measured in the geographic reference frame. Prior to the processing of the ground data with R-SCHA, their locations and the components X and Z

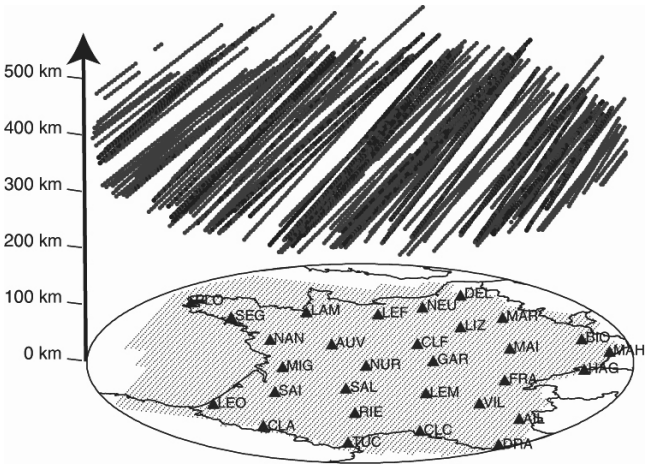

Figure 2. Data distribution over France and repeat stations: observatory data (solid triangles), aeromagnetic data (dots), and CHAMP satellite data (solid circles).

must be rotated in the geocentric reference frame. We use the WGS84 ellipsoid to convert the data. Considering the spatial resolution in the present work, any ellipsoid is appropriate as changing the ellipsoid is equivalent to displacing the repeat stations by a few tens of meters. When representing the magnetic field at the ground surface, we have to convert the R-SCHA model back to the geodetic reference frame. The lowest altitude recorded in the data set is $E = -5.634$ km at the northern repeat station DEL (Delette in Figure 2) and the lowest elevation is therefore defined at $E_{\min} = -6$ km in the geocentric reference frame.

[11] Modeling the secular variation at a regional scale remains a difficult issue. The secular variation is mainly a large-scale feature, much larger than the region under study. As a result, its representation requires a number of local parameters that the number of repeat stations cannot afford. Using R-SCHA does not necessarily provide a better representation of the secular variation but, to the contrary, creates artificial oscillations or edge effects. The short time period covered by the satellite data is also problematic and other satellite data missions would be necessary to fill this gap. We are aware that using a global secular variation model in order to reduce the data sets may introduce a bias, but at the present stage,it remains the best option. Moreover, we illustrate in Figure 3 that by using this compromise we do not significantly alter the consistency between repeat stations and aeromagnetic data. A global model covering the time window of the magnetic measurements needs to be subtracted from the data. Instead of using Definitive Geomagnetic Reference Fields (DGRF) models from 1960 onward, we use the CM4 Comprehensive Model [*Sabaka et al.*, 2004]. It extends from 1960 to mid-2002 and the maximum secular variation degree $n = 13$ is very convenient for the present study. Moreover, the secular variation evaluated from CM4 is smoother with time and more consistent with the Chambon-La-Fôret (CLF) annual means than DGRF models, which are, to the contrary, less smooth and less accurate. The procedure is not perfect and despite

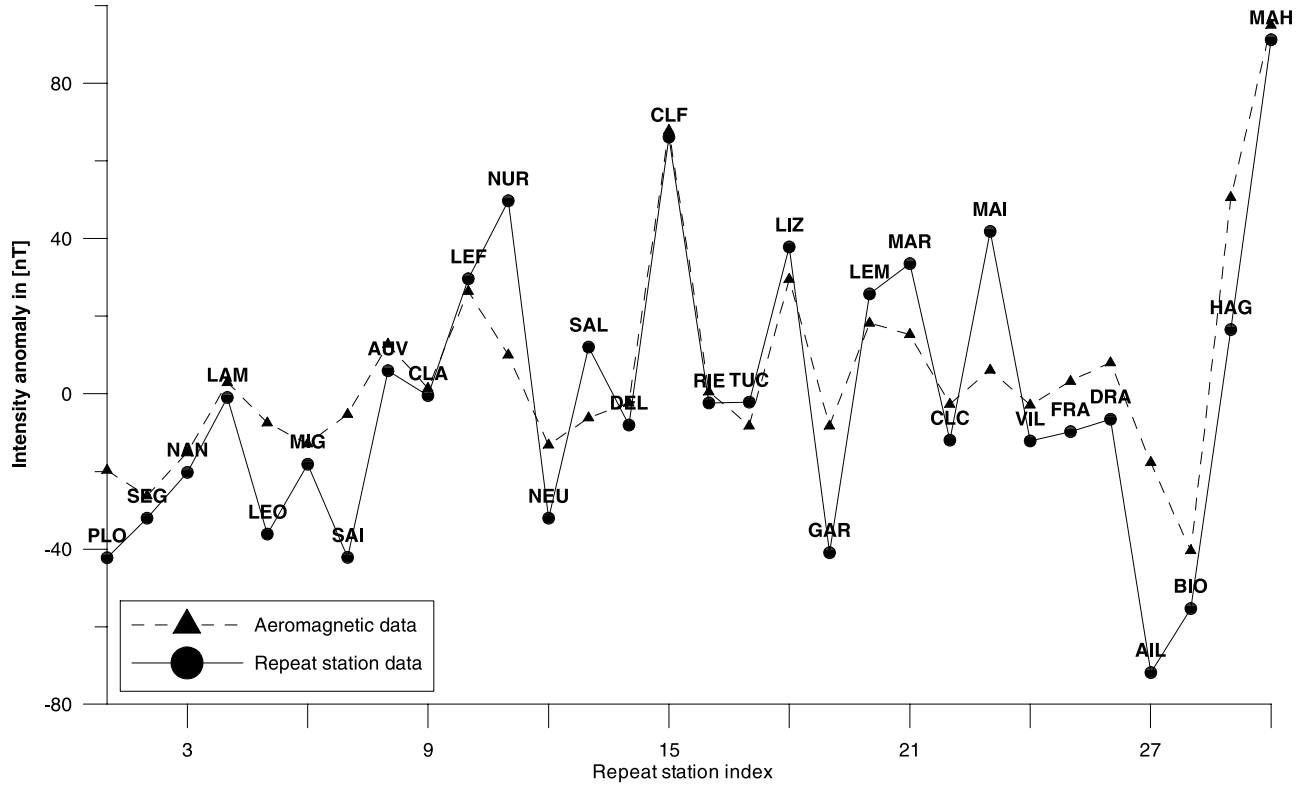

Figure 3. Comparison between the intensity anomaly calculated at the repeat stations (solid line) and the aeromagnetic intensity evaluated at the same locations with aeromagnetic data (dashed line). Repeat stations are ordered by longitude, from west to east.

the great improvement of CM4 over the DGRF models in the secular variation reduction some peculiarities remain. For instance, a comparison between CM4 model and the repeat stations data shows that CM4 has time edge effects near 1960 and 2002. Because a large uncertainty is inherent in repeat stations data, we further checked the consistency of the model with the monthly mean values provided by the three German observatories at Niemegk (NGK), Fürstenfeldbrück (FUR) and Wingst (WNG). In general, the time edge effects can be observed throughout Europe using yearly mean values computed at European observatories. Keeping in mind this failure, we subtract CM4 global field from the repeat stations up to degree and order 15 for the core field and up to 13 for the secular variation. Indeed, *Cain et al.* [1989] showed that significant contributions of the core may remain up to degree 15, and some authors now represent the lithospheric field from degree 16 only [*Maus et al.*, 2006]. For each repeat station, the complete time series between 1965 and 2000 is analyzed and a standard deviation is estimated for each of the residual field components. In average, the data uncertainty is about $\overline{\sigma} = 7.5$ nT, when considering all repeat stations and all components, with a maximum of 17.5 nT at Marlenheim (MAH) and a minimum of 4.4 nT at Lizy-sur-Ourcq (LIZ). We consider the average value of the repeat station and observatory data over the time range 1965–2000. Finally, 29 averaged vector data and 1 averaged vector observatory data, almost equally distributed at the ground, were available and reduced.

3.2. Aeromagnetic Data

[12] *Le Mouël* [1969] published the charts for the geomagnetic field components over France, which were derived from aeromagnetic total intensity measurements and a few vector measurements in the repeat stations network. The French territory was flown over an altitude of 3 km above the sea level along north-south profiles spaced 10 km apart. The estimated precision of the intensity measurements is 4 nT in absolute value [*Galdeano et al.*, 1980]. Here we do not consider the raw data but the grid of intensity data to the year 1964.5. The grid was formerly constructed using the Cartesian Lambert II étendu coordinate system [*Le Mouël*, 1969]. We thus convert the data locations from Lambert to the geodetic WGS84 reference frame, then to the geocentric reference frame; intensity values remain invariant by rotation. There are 7396 total intensity measurements considered in this study, which are near-homogeneously distributed near the lowest surface. Gaps following the French political boundaries can still be seen in the southern, eastern and the northern part of the spherical cap (Figure 2). In the present work, we do not consider aeromagnetic data in neighboring countries mainly because stitching together different compilations introduces discontinuities and an incoherent large-scale pattern. In the future, consistent compilations will be available over Europe that will be helpful to alleviate the problem of data gaps near the edges. We apply the same procedure as that for the repeat stations data and subtract the core field intensity up to degree 15 predicted by the CM4 model for the year 1964.5. As for the repeat stations, intensity anomaly data are now assumed to contain static and lithospheric field only.

[13] A simple check is carried out in order to verify the compatibility between the aeromagnetic and repeat stations anomaly intensities after reduction of a core field and a secular variation model. For these two different data sets, being barely 3 km apart in altitude, a direct comparison is made. The aeromagnetic data inside a small circle of radius 0.1° centered on the position of a given repeat station is averaged and compared with the mean repeat station intensity value between 1965 and 2000. The consistency between the two data sets is in general satisfactory. The standard deviation between the two curves is $\sigma \simeq 19$ nT, with a maximum difference of 51 nT at Ailefroide (AIL) and a minimum of 2nT at CLF (see Figure 3). There is no apparent correlation between these differences and the repeat stations altitude. For instance, AIL is closer to the aeromagnetic data (1.5 km above see level) than CLF observatory (0.2 km above see level) but the mismatch is larger. Apart from the rough methodology used, which does not take into account the rapid decreasing intensity of very local anomalies with altitude, there are several possibilities that can account for the incompatibilities observed with some repeat stations; for example Léon (LEO), Saint Emilion (SAI), Garchy (GAR) or Aillefroide (AIL).

[14] The repeat stations are prone to measurement and reduction errors that are the principal source of discrepancy. External field contributions are difficult to remove and the repeat stations are reduced using the time variations recorded at the nearest observatory. Spatial and temporal variations of the field are therefore not fully taken into account. Considering the number of data, recorded every 5 years, taking the mean between 1965 and 2000 may not be completely statistically representative either. Moreover, some repeat stations lie on local magnetic anomalies (for example GAR). Last but not the least, the larger difference observed is at AIL, which lies in the Alp mountains where for evident reasons, the aeromagnetic survey was carried out at 5 km of altitude. The downward continuation to 3 km may also be a source of discrepancy between this particular station and the aeromagnetic data.

[15] Some second-order errors also contribute to the mismatch between the anomaly intensities for aeromagnetic and repeat stations. As mentioned above, aeromagnetic data may suffer from the CM4 time edge effects near 1964.5 (see section 3.1). In addition, the secular variation contributions from degrees higher than 13, not modeled in CM4, may bias the mean value of the average calculated at the repeat stations. Also, finally, CM4 model ignores long-term induction produced by the lithospheric conductivity anomalies. At present, we assume the field to be purely static but, although this is controversial and probably a high-order error, the induced lithospheric field may slightly change with time.

3.3. Satellite Data

[16] In July 2000, the Earth orbiting satellite CHAMP was launched and its circular, near-polar orbit, makes it suitable for detecting lithospheric signals. Because of its low orbit, CHAMP is also closer to the ionospheric sources and special efforts to remove the external contributions are required. Moreover, CHAMP suffers from misalignments between the star imager and the vector magnetometer. Careful data selection and corrections play a key role in determining the lithospheric field and the experience gained over the 5 years of CHAMP activity has resulted in a series

of effective adjustments and corrections in its data processing. The corrected data are now of high-quality and field models from CHAMP have become increasingly stable and reliable [*Maus et al.*, 2006]. The accuracy of these magnetic measurements provides unprecedented precision in investigating the lithospheric field.

[17] Almost 5 years of CHAMP scalar and vector data from August 2000 to January 2005 are used in the present study for which the data selection procedure is described in detail by *Maus et al.* [2006]. Data are selected for quiet periods with $K_p \leq \mathbf{2}$ and a maximum of $K_p = 2.5$ for the previous three hours from the local time sector 0000 to 0500 LT. The maximum $|D_{st}|$ index chosen is 50 nT and $|dDst/dt| = 3$ nT per hour. Star camera misalignment is also corrected and a preliminary external field is removed from the data, as well as external quadrupoles. A secular variation model is estimated from the data and removed for the central epoch using a POMME 2.5 model [*Maus et al.*, 2005]. Data are corrected for the polar electrojet [*Maus et al.*, 2006] and for an ocean tidal model [*Tyler et al.*, 2003]. In order to be consistent with ground and aeromagnetic data reduction, we subtract a CM4 internal core field model up to degree $n = 15$ [*Sabaka et al.*, 2004] so that it is predominantly the lithospheric field that remains. The selection and the reduction procedures yield 6413 scalar data and 2166 vector data distributed between 350 and 480 km altitude.

4. Inverse Problem

[18] Prior to being processed, all the data are rotated from the geocentric reference to the cone reference frame centered on the geocentric coordinates(Φ, Θ) (see Figure 1). Rotation formula are derived from standard spherical trigonometry and are given by *De Santis et al.* [1996].

[19] As already noted, all measurements of the magnetic field $\mathbf{B}_m$ and the intensity F_m are reduced using the secular variation and the CM4 core field models. We adjust the regional magnetic field $\delta\mathbf{B}$ defined by (9), and the anomaly intensity δF defined by (10). The components δX, δY and δZ of the residual field $\delta\mathbf{B}$ are expressed using equations (5), (6) and (7). According to these equations, any scalar or vector values of the observed magnetic field $\mathbf{d}$ can be linked to the parameter set $\mathbf{g}$ through a nonlinear function f such that

$$\mathbf{d} = f(\mathbf{g}) + \varepsilon \tag{11}$$

where the vector $\mathbf{g}$ includes all parameters $\{G_p^m,\ H_p^m\}$, $\{G_{n_k}^{m,i},\ H_{n_k}^{m,i}\}$ and $\{G_{n_k}^{m,e},\ H_{n_k}^{m,e}\}$ and the error ε is assumed to be Gaussian. We search for a set of Gauss coefficients $\mathbf{g}$ minimizing the functional χ^2 defined by

$$\chi^2 = \|\mathbf{d} - f(\mathbf{g})\|^2 + \alpha\|\delta B\|^2 \tag{12}$$

[20] This means we seek a solution in the least squares sense with a roughness constraint. The roughness is quantified by the norm of the magnetic field itself and the scalar α, which is to be adjusted in order to determine the best compromise between the data fit and the model roughness. Thanks to the orthogonal properties of the local basis functions, the norm can be shaped into a diagonal matrix $\mathbf{E}$ giving the amount of energy per coefficient [*Thébault et al.*, 2006]

$$\|\delta B\|^2 = \mathbf{g}^T\mathbf{E}\mathbf{g} \tag{13}$$

Setting the derivative of (12) with respect to $\mathbf{g}$ gives

$$\alpha\mathbf{E}\mathbf{g} = \mathbf{A}[\mathbf{d} - f(\mathbf{g})] \tag{14}$$

where the matrix $\mathbf{A}$ is the Frechet derivative matrix of f, whose elements are $A_{i,j} = \frac{\partial f_i}{\partial g_j}$ relating the vector of model parameters $\mathbf{g}$ to the vector of observations $\mathbf{d}$.

[21] When the function f is nonlinear, equation (14) is solved by an iterative process. The Newton-Raphson iterative procedure requires a first guess solution $\mathbf{g}_0$ minimizing (12). Then, expanding the function f to a first-order Taylor series around $\mathbf{g}_0$ and refining i times the solution yields

$$\mathbf{g}_{i+1} = \mathbf{g}_i + \left(\alpha\mathbf{E} + \left(\mathbf{A}^T\mathbf{A}\right)_i\right)^{-1}\left(\mathbf{A}_i^T(\mathbf{d} - f(\mathbf{g}_i)) - \alpha\mathbf{E}\mathbf{g}_i\right) \tag{15}$$

[22] The next step, although not mandatory, is to linearize the function f. Assuming that the direction between the global and the lithospheric fields remained unchanged between 1964.5 and 2000, the lithospheric field anomaly intensity δF can be well approximated by

$$\delta F \simeq \frac{\delta B.\mathbf{B}_c}{\|\mathbf{B}_c\|} = \frac{\delta X.X_c}{F_c} + \frac{\delta Y.Y_c}{F_c} + \frac{\delta Z.Z_c}{F_c} \tag{16}$$

where $\boldsymbol{\delta B}$ is the crustal field and B_c a core field model. The three components X_c, Y_c, and Z_c are derived from the CM4 model to degree and order 15. The inverse problem being now linear, we write $f = \mathbf{A}\mathbf{g}_i$, with $\mathbf{A}$ independent of $\mathbf{g}$. Therefore equation (15) simply becomes

$$\mathbf{g} = \left(\alpha\mathbf{E} + \mathbf{A}^T\mathbf{A}\right)^{-1}\mathbf{A}^T\mathbf{d} \tag{17}$$

[23] The validity of the approximation (16) depends on the magnitude and the direction of the residual field $\delta\mathbf{B}$. Its consistency is verified using the repeat stations and the observatory magnetic data. In the present scenario, the maximum absolute difference between the true intensity anomaly $\delta\mathbf{F}$ and the approximation (16) is negligible and never exceeds 0.2 nT. This test depends on the location of the repeat stations and ignores the large anomalies that may exist elsewhere. In regions with lithospheric field magnitudes larger than 1000 nT, or if the unknown angle between $\mathbf{B}_c$ and $\mathbf{B}_m$ is suspected to be important, the solution (16) fails as a good approximation and the iteration process (15) should be preferred. In the present work, we have checked that the CM4 model is reliable, that the core field is almost fully removed from the data and that the French territory does not exhibit magnetic anomalies greater than a few hundred nanotesla at ground level. Consequently, the linear approximation given by equation (16) and leading to the inverse problem (17) is retained.

4.1. Truncation and Maximum Resolution

[24] In theory, the series (5), (6), and (7) are infinite. In practice, regarding the number of data and their distribution,

Table 1. Standard Deviation, Residual Mean Square, and Correlation Factor Before and After Filtering Out the Wavelengths Smaller Than $\lambda = 40$ km in the Aeromagnetic Data Set

	σ, nT	RMS_{Aero}, nT	RMS_{RS}, nT	RMS_{sca}, nT	RMS_{vec}, nT	R
Unfiltered data	8.9	12.4	20.6	0.6	0.9	0.88
Filtered data	1.9	1.7	21.3	0.6	0.8	0.98

the maximum spatial indices K_{max} (not to be confused with the conical functions) and P_{max} (not to be confused with the Legendre functions) may be chosen according to several criteria. We define two maximum indices K^i_{max} and K^e_{max} for the truncated series related to the coefficients $\{G^{m,i}_{n_k}, H^{m,i}_{n_k}\}$, and $\{G^{m,e}_{n_k}, H^{m,e}_{n_k}\}$, respectively.

[25] Near its lowest surface, the cone is densely covered by an almost uniform data distribution and a large series expansion is allowed. According to the shape of the radial functions $(a/r)^{n_k+1}$ in equation (2), the corresponding Legendre basis functions will contribute mainly in the lower half part of the cone (but not negligible in the upper half). A maximum index expansion of $K^i_{max} = 30$ is chosen. It corresponds roughly to a minimum wavelength representation of $\lambda_{min} = 40$ km at the Earth mean radius. Solving the aeromagnetic data to their 10 km resolution requires an expansion index $K^i_{max} = 110$ [*Thébault et al.*, 2006] but the corresponding number of Gauss coefficients is difficult to reach by the inverse problem.

[26] The coefficients $\{G^{m,e}_{n_k}, H^{m,e}_{n_k}\}$ must be included in the modeling, even if the field is only internal [*Thébault et al.*, 2006]. According to the shape of the radial basis functions $(r/a)^{n_k}$ in (2) the Gauss coefficients $\{G^{m,e}_{n_k}, H^{m,e}_{n_k}\}$ have a higher contribution in the upper part of the cone (but not negligible in the lower part). The coefficients $\{G^{m,e}_{n_k}, H^{m,e}_{n_k}\}$ will account for the modeling of the magnetic field at intermediate and satellite altitudes and some large wavelengths at the ground level. Since the CHAMP satellite flies at an average altitude of 400 km, it is generally believed that wavelengths smaller than 400 km are not detected. As a result, high resolutions at high altitudes are not necessary and we opt for a maximum truncation index $K^e_{max} = 10$. This choice offers a maximum spatial resolution of 270 km.

[27] The determination of the truncating index P_{max} is difficult and must be done carefully as the conical basis functions are essential for the regional model upward/downward continuation. The better these parameters are determined, the better the predictions at intermediate altitudes. The conical basis functions contribute to the three components of the magnetic field and are required to properly fit the data at all altitudes. A low truncation index P_{max} penalizes the vertical representation of the magnetic field and the reliability of the model near the edges [*Thébault et al.*, 2006]. Unfortunately, the general vertical distribution of the data inside the cone shows mainly two regions separated by a large gap of 350 km length (see Figure 2). The radial constraint of the model is poor and we cannot expect a very good detection of the magnetic field radial variations. The choice of $P_{max} = 10$ is a good trade-off between the data resolution, the proper field representation with altitude, and the conditioning of the inverse problem.

[28] For the Mehler expansion we set $M_{max} = 10$, for the "internal" Legendre expansion, $M_{max} = 30$ and for the "external" expansion $M_{max} = 10$. This represents an amount of 1166 coefficients to be coestimated. The inverse problem is also regularized by minimizing the norm of the lithospheric magnetic field inside the cone. In order to estimate the parameter α in (17) that will allow the best prediction of the model at intermediate altitudes, we apply our algorithm on synthetic data first. Using CM4 vector and scalar anomaly values on actual data locations, we study the correlation factor between the expected magnetic field and the R-SCHA prediction between the altitudes 100 and 300 km. Setting $\alpha = 1e^{-6}$ in equation (17) for the internal Legendre basis functions and $\alpha = 9e^{-7}$ for the Mehler Basis functions provides the best trade-off between the fit, the smoothness of the model near the edges, and the reliability of the gap prediction. The average correlation factor is 0.90 at intermediate altitude for the synthetic case. Note that in the real case, we cannot ascertain the reliability of the model at intermediate altitudes because the data are noisy and not fully compatible. The same weight was applied to the different data sets in the inversion. Some of the estimated parameters may not be significant but since no severe singularity occurs in the inversion of the resolution matrix $C = (\alpha\mathbf{E} + \mathbf{A}^T\mathbf{A})$, we keep all of them. Moreover, removing some statistically insignificant parameters is consistent only if the data are resolved up to the noise level. If this is not the case, removing some coefficients will carry the risk of introducing a further anisotropic effect, more significant than the one introduced when considering different truncation indices for the expansion of the basis functions. This may have unfortunate consequences on magnetic map interpretation.

4.2. Model Statistics and Validation

4.2.1. Statistics

[29] Two different inversions are undertaken. Their respective statistics are summarized in Table 1. We first consider all data without further processing. Then, in a second step, we filter out the wavelengths larger than 40 km in the aeromagnetic data. These low-pass-filtered data are expected to be more consistent with the maximum resolution and the truncation indices previously defined.

[30] In the first experiment, the residual mean square RMS_{Aero} is not in agreement with the estimated aeromagnetic data accuracy (section 3.2) and indicates some unmodeled signal. For the repeat stations (RS) data, the RMS_{RS} estimated by R-SCHA is also greater than the value estimated by the independent statistics made on the repeat stations alone (section 3.1). This could indicate either a lack of fit on the data or an incompatibility between aeromagnetic and repeat stations data at some locations (see Figure 3). At last, the satellite RMS_{Sat} is satisfactory for both the vector and the scalar data. It shows the high quality of the data and the ability of the regional model to represent them. The overall correlation factor between the data and the prediction in this first inversion is $R = 0.88$.

[31] Using aeromagnetic filtered data, the fit is improved because the data information content and the modeling

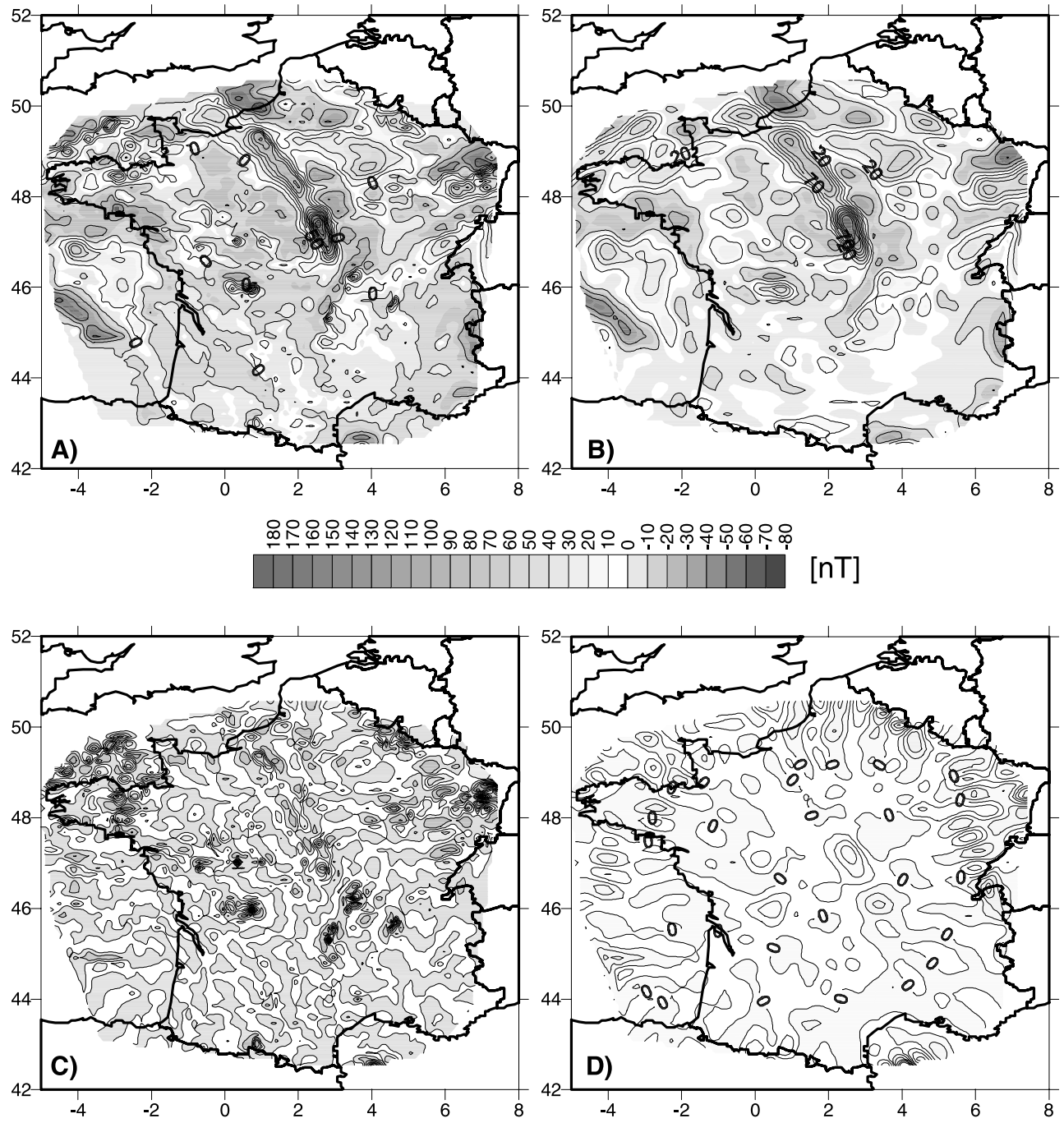

Figure 4. (a) Anomaly intensity (contour lines are 10 nT); (b) predicted anomaly intensity (contour lines are 10 nT); (c) Difference between real and predicted anomalies (contours lines are 10 nT); (d) same as Figure 4c but low-pass filtered for wavelengths greater than 40 km (contour lines are 2 nT).

resolution are now more consistent (see Table 1). This also has a direct effect in the estimation of the overall correlation coefficient $R = 0.98$. The fact that the RMS_{RS} is slightly larger is likely due to the fact that some repeat stations, located on local anomalies, are now less consistent with aeromagnetic data since these small-scale anomalies are removed. Note that RMS_{Sat} does not vary significantly since small wavelengths are not detected at satellite altitudes.

[32] Interestingly, the different sets of parameters obtained by least squares on the nonfiltered data first, and then on the low-pass-filtered data, have a good correlation factor of $R = 0.92$. A comparison showed that mainly Legendre coefficients associated to short wavelengths are changed while the values of other coefficients, accounting for larger wavelengths, remain nearly constant.

4.2.2. Residual Analysis Between Predicted and Observed Data

[33] Figure 4 illustrates the comparison between the grid anomaly intensity data (Figure 4a) and the predicted intensity anomaly (Figure 4b). The residuals (Figure 4c) and its low-pass-filtered data (Figure 4d) are also sketched.

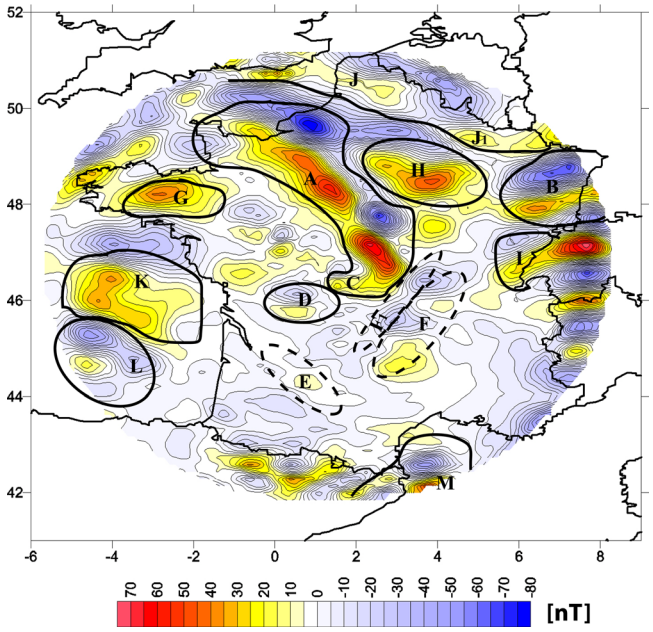

Figure 5. Predicted X component of the residual field at the mean Earth radius. Contour lines are 5 nT. The letters refer to anomalies discussed in text.

[34] The comparison between the data and the predicted intensity anomaly maps shows good agreement between the measurements and the model in shape and intensity. The predicted anomaly map is smoother than the aeromagnetic data grid. Indeed, for practical reasons we limited the series expansions and chose to regularize the inverse problem; both processes acting like a low-pass filter. This low-pass-filtering effect is illustrated by the residual map (Figure 4c), which shows very small shapes and localized peaks that are not retained in the modeling.

[35] In order to verify that the residuals between the nonfiltered aeromagnetic grid and the model may be explained by the series truncation, we filter out the wavelengths smaller than 40 km in the residual map (Figure 4c). The resulting map (Figure 4d) should be zero everywhere if both processes were perfectly equivalent. Note that in theory, this is not completely true because the definition of cut frequency and minimum wavelength is an approximation in regional modeling [*Thébault et al.*, 2006]. In the cap center, truncating the series and filtering the data is almost equivalent: the residuals have no special features and are less than 5 nT. Near the edges, the residuals have the same amplitude but oblong shapes are noticeable everywhere near the boundaries that have spatial extensions greater than 40 km. The circular and symmetric aspect of this remaining signal shown in Figure 4d is typical when truncating the conical basis functions to low P_{max}. Since the Mehler functions is maximum near the lateral edges, the field is slightly distorted. It also explains the lack of fit of the data in these regions [*Thébault et al.*, 2006]. Quantifying the approximation made at the edges will be important in the future if we want to patch together several local models to cover larger areas.

5. Lithospheric Magnetic Model Over France

[36] Using the 1166 local parameters we calculate the forward problem over a dense regular grid with a distance of 16 km between two points. Figures 5, 6, and 7 show the lithospheric magnetic model at the mean Earth radius. The features in France agree well with the known geological features but as will be shown, a few anomalies located near the edges appeared to be artifacts. In general, despite the care taken to solve the inverse problem, extrapolation of the

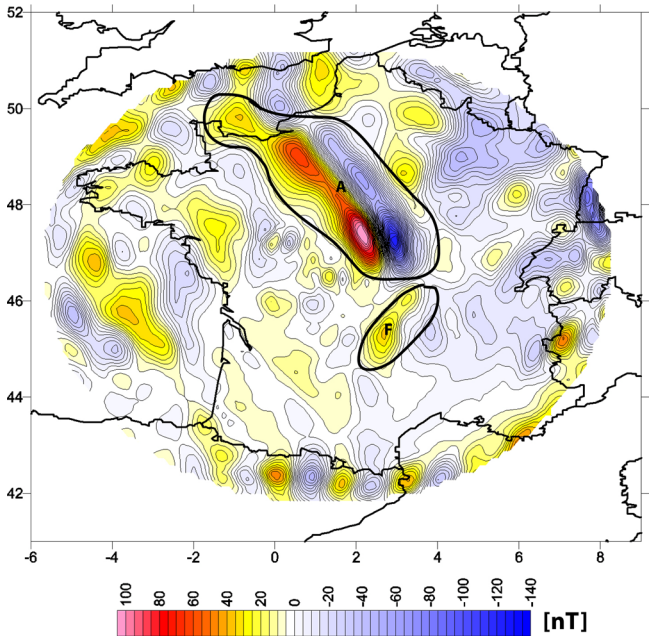

Figure 6. Predicted Y component of the residual field at the mean Earth radius. Contour lines are 5 nT.

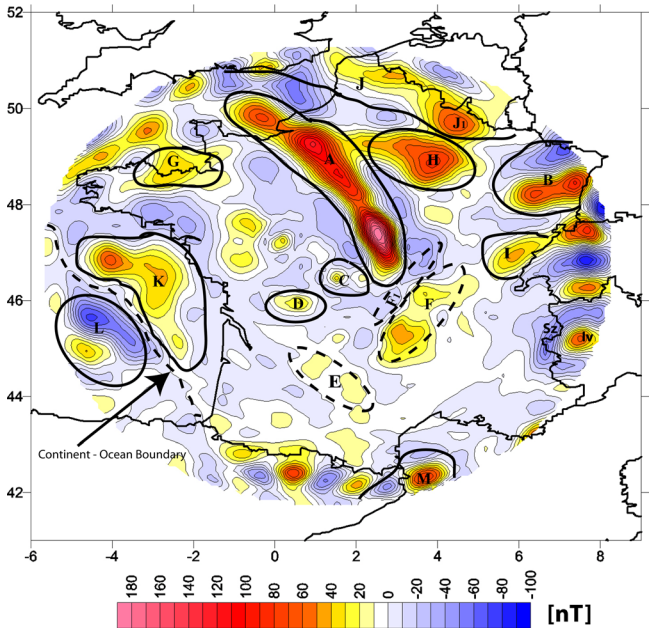

Figure 7. Predicted Z component of the residual field at the mean Earth radius. Contour lines are 10 nT.

model beyond the area covered by data should be considered carefully. To the contrary, interpolation seems to always be a stable process.

5.1. Geological Interpretation

[37] In the following, we outline the correlations between the anomaly maps and the known geological structures. Apart from the anomalies observed in the Bay of Biscay and in the Valencia Gulf, they are due to structures located in the Variscan or older continental lithospheric basement. Detailed interpretations may be found in the report accompanying the aeromagnetic maps of France published by the Bureau de Recherches Géologiques et Minières [*Corpel et al.*, 1972]. Several papers summarize the current knowledge for the prealpine basement of western Europe [e.g., *Edel and Weber*, 1995]. They emphasize the difficulty of deciphering these old structures as most of the Paleozoic basement is hidden by a sedimentary cover.

[38] Generally, the anomalies are better identified on the X and Z maps, and therefore we focus the discussion on these components. This behavior is due to the predominant E-W trending of the structures [*Edel and Weber*, 1995]. In this qualitative interpretation, keeping in mind the general aspect of vertical (respectively horizontal) field anomalies of a dipole type structure, the Z component anomalies is characterized by a central positive area, surrounded by a negative rim, whereas the X component anomalies are characterized by a positive area to the south and a negative area to the north [*Corpel et al.*, 1972]. Let us now briefly describe the main anomalies, referred to by capital letters on Figures 5, 6, and 7.

[39] Anomaly A is the most striking, well-known anomaly, so-called Paris basin anomaly. It may be suspected, according to Figure 5, that its southern end extends into a small E-W structure (see anomaly C). Each of the three maps shows that the anomaly is fairly two-dimensional, although its intensity decreases northwestward, due to the deepening of the basement. The nature and composition of the structures are still unknown [*Pham et al.*, 2000].

[40] Anomaly B is a signature of Visean intrusive and calc-alkaline volcanics which partly outcrop in the northern Vosges. This anomaly is a good example illustrating the difference between the Z and the X component anomaly. The maximum of the Z anomaly is roughly above the geological sources, whereas the X anomaly clearly comprises two parts, a positive anomaly shifted southward with respect to the Z maximum, and a negative anomaly shifted northward. The maximum gradient strip coincides with the Z maximum. This anomaly can hardly be seen on the Y map.

[41] Anomalies C, D, and E are associated to a dioritic complex around the Limousin. In the area C, in the north, a dotted line of magnetic diorites outcrops along the Marche fault; the Z map, as well as detailed aeromagnetic maps suggest a connection of these rocks with the southern extension of the sources of the Paris basin anomaly. The anomalies D and E are due to the tonalites of northwestern and southern Limousin, respectively.

[42] Anomaly F can be linked to Devono-Dinantian magmatism, of the Autun and Roanne basins in the eastern part of the Massif Central. The SSW-NNE trending negative anomaly to the west corresponds to the Sillon Houiller a prominent strike-slip fault which bounds the eastern Massif Central (F1, in Figure 7).

[43] Anomaly G refers to the Cadomian complex of northern Brittany. The known extent of this geological unit around the bay of Saint Brieuc is in good agreement with its magnetic anomaly. This unit may be the western extension of the Bohemian/Cadomian terrane west of the Bray fault [*Edel and Weber*, 1995].

[44] Anomaly H which is associated with magmatic rocks, of uncertain age, assumed Paleozoic or upper Proterozoic; the northern axis of the anomaly coincides with the boundary between Rhenohercynian and Saxothuringian zones which resulted from the closing of the Rhenohercynian ocean in the Carboniferous.

[45] Anomaly I, the anomaly of the Massif de la Serre, is only known to be partly magmatic and is likely Variscan in age.

[46] Anomaly J, the large complex of Ardennes structures, is of early Paleozoic in age and J1 is related to magmatic rocks which intruded the Cambrian Rocroi massif.

[47] Anomaly K represents the metamorphic structures of the continental plateau.

[48] Anomaly L is situated on the well-known oceanic structures of the Bay of Biscay and results from its opening.

[49] Anomaly M is connected with the opening of the Valencia Gulf.

[50] Other major anomalies are visible near the French border. In Switzerland and in northern Italy, for instance, the model may be spurious and these inconsistencies may also impinge on the Alsace region. In the western Alpine Belt, we distinguish a clear negative magnetic anomaly over the Ivrea-Verbano zone along the complete length of the western Alpine suture zone (Sz in Figure 7). This anomaly is genuine and present in the aeromagnetic data set. Interestingly, outside the data limits, the model seems to predict the positive anomaly over the Ivrea body in northern Italy (Iv in Figure 7). Nevertheless, we suggest to use these extrapolations with caution as the anomalies may be hidden by edge effects or may simply be not relevant. In Switzerland, for instance, compared with existing anomaly maps [*Wonik et al.*, 1992], the large positive and negative anomalies seem to result from artifacts.

[51] Let it be reminded that in this paper, the minimum wavelength of the magnetic anomalies calculated with the R-SCHA expansion is 40 km at the mean Earth radius. Thus this kind of regional modeling is intermediate between global lithospheric field modeling and detailed local surveys. It seems difficult to reach the short wavelengths of detailed surveys with R-SCHA expansion but the loss of detail is compensated by the calculation in terms of vector fields which may be easily computed at every altitude between ground and satellite levels. Thus the advantages of upward continuation for a more quantitative interpretation could be fully exploited. The knowledge of the vector anomaly field is another advantage over local surveys, which are mostly restricted to total field measurements reduced to a fixed altitude.

5.2. Prediction With Altitude

[52] Figure 8 shows a few sketches of the predicted Z component with varying altitude, from ground to satellite.

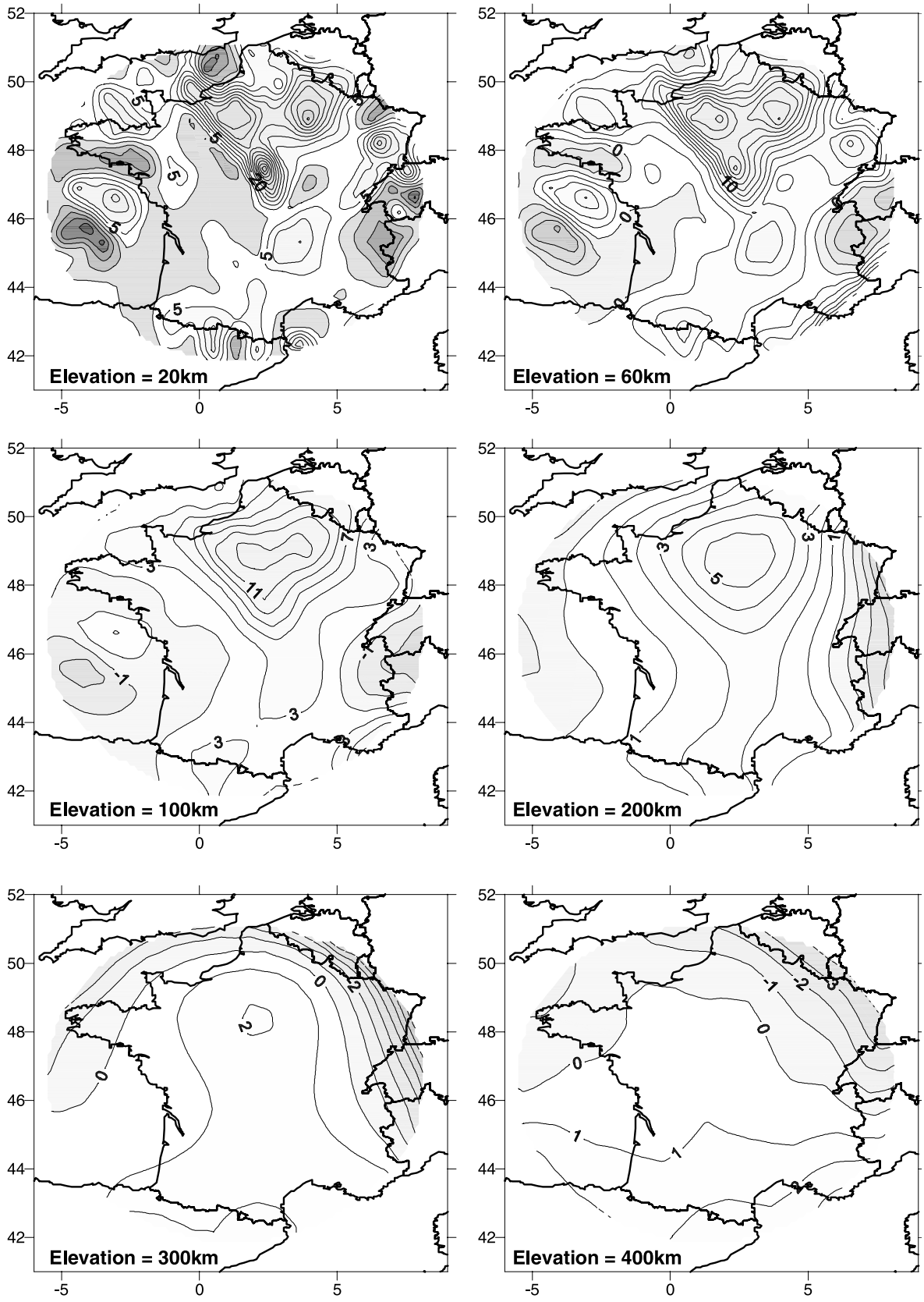

Figure 8. Prediction of the Z component residual field with altitude. At 20 km most of the small features are still visible (contour lines are 5 nT). Between 60 and 100 km altitude, only larger wavelengths remain (contour lines are 2 nT). Above 200 km the Paris basin anomaly is displayed but weak and is no more detectable between 300 and 400 km altitude (contour lines are 1 nT). From about 400 km altitude, the local model agrees well with global crustal models.

The predicted model concurs well with the behavior expected from a anomaly field of lithospheric origin. The magnetic anomalies and their amplitudes quickly decay and small features rapidly coalesce with altitude. At 100 km altitude we do not distinguish between anomalies from the Paris basin and adjacent areas. The footprint of the Paris basin anomaly, being still visible at 100 km, indicates that it has a deep-rooted structure although the main source of this anomaly probably lies at an average depth of 7 km [*Le Mouël*, 1969; *Pham et al.*, 2000]. A systematic investigation of the magnetic maps at different altitudes shows that no main anomalies are detectable above 120 km. Although data were not available at these intermediate altitudes (Figure 2), the interpolation model is realistic and informative.

[53] One peculiarity still remains around 300 km altitude. We notice a slight direction change in the radial component. Thanks to the regularization, we do not observe a strong lateral boundary effect, nevertheless, the poor determination of the Mehler coefficients, which control the behavior of the modeling with altitude, could induce this small magnetic model inflation noticeable near the lateral boundaries. This effect is absent when processing a set of consistent synthetic data and another hypothesis is plausible: Since this pattern starts around 300 km altitude, what we observe could partly be a manifestation of the data spectral gap. At 400 km altitude, the field is well represented and is consistent with global lithospheric models, especially with MF4 crustal model [*Maus et al.*, 2006].

[54] The general altitude variations for the model is encouraging. In the future, we hope that the origins of the magnetic sources can be further investigated by examining the altitude variation of the field. To some extent, this information is concealed in our model and it represents a strong incentive to carry out more work on spectral analysis to unravel this valuable information.

6. Conclusions

[55] The revised spherical cap harmonic analysis was motivated by the inability of the original SCHA to cope with the processing of data collected at various altitudes. It was shown by *Thébault et al.* [2006] that the failure comes from an inappropriate choice of the basis functions, which was, in fact, incomplete. This paper reports the first application of the new theory to a real situation using the availability of ground, aeromagnetic and satellite data over France. Besides the test of R-SCHA, our aim was to describe the spatial characteristics of the lithospheric field over the whole altitude range, despite the very heterogeneous data distribution. The distribution is uneven with altitude, as illustrated in Figure 2 but also horizontally and yet, the regional model is realistic within the conical domain. Unfortunately, the sparse ground repeat stations network and the dense aeromagnetic data being restricted to field intensity, we cannot reach a complete and faithful description of all data sets. We thus restricted ourselves to a minimum wavelength representation of 40 km at ground level by truncating the series expansions. The loss of information does not hinder the identification of the detailed anomalies connected to known geological features; moreover, it is compensated by the modeling of the anomalies in terms of a full vector field. Despite some slight peculiarities, the variation with altitude is quite sensible and shows clearly which information is generally lost when one moves away from the sources. This last result demonstrates the superiority of a regional modeling over a global modeling for delineating small-scale details of the lithospheric field, when a dense set of data is available over a limited area.

[56] Let us stress again that R-SCHA is a representation unable to separate the different contributions of the field. Presently, the only way of removing the true external field is a careful data selection. As it is classically encountered with a bounded domain, the influence of the internal sources located outside the selected region is difficult to estimate and thus to eliminate. As a result, we cannot completely ascertain weather the regional model over France is not somehow contaminated by these neighboring sources. In addition, we should not forget that the data do not yet allow the generation of a complete regional model because wavelengths between 200 and 400 km are not properly sampled by the available data. We suspect the effect of this well-known spectral gap in our model around 300 km altitude. Other measurements at balloon or spy plane altitudes could help to better constraint the model radially but, unless they have a good spatial coverage, they will probably not fill the spectral gap. To the contrary, the configuration of the Swarm mission is designed to address this issue by measuring the horizontal gradient of the magnetic field. The results shown here suggest that with a consistent data set, the entire crust can be accessed by the R-SCHA method. Using the higher resolution Swarm data combined with aeromagnetic data will provide the first ever regional models for the lithospheric field at scales from 30 to 3000 km and will help us to access the complete lithospheric depth.

[57] Another step forward will be to stitch together regional models in order to obtain accurate vector magnetic maps for larger regions. For this purpose we will use at the same time, marine, ground survey, repeat stations and observatory data together with aeromagnetic and satellite data. Many regions are not accessible to direct investigation and mapping the magnetic field is one of the most efficient ways to unravel the structure and the geological history of the Earth. Therefore R-SCHA seems to be a good candidate for high-resolution lithospheric field modeling in those regions.

[58] **Acknowledgments.** We would like to thank Jean-Bernard Edel for his substantive comments about the geology of France and Stefan Maus for providing the CHAMP satellite data. We also acknowledge the comments of Angelo De Santis and an anonymous referee that helped to improve the manuscript.

References

Alldredge, L. R. (1981), Rectangular harmonic analysis applied to the geomagnetic field, *J. Geophys. Res.*, *86*(B4), 3021–3026.

Cain, J. C., Z. Wang, D. R. Schmitz, and J. Meyer (1989), The geomagnetic spectrum for 1980 and core-lithospheric separation, *Geophys. J.*, *97*, 443–447.

Corpel, J., M. Ogier, and C. Weber (1972), Carte Magnétique de la France 1/1,00,0000, feuille nord—Anomalies du champ total, Bur. de Rech. Géol. et Min., Orléan, France.

De Santis, A., J. M. Torta, and C. Falcone (1996), A simple approach to the transformation of spherical harmonic models under coordinate system rotation, *Geophys. J. Int.*, *126*, 263–270.

Edel, J. B., and K. Weber (1995), The cadomian terraned, wrench-faulting and thrusting in the central Europe variscides— Geophysical and geological evidences, *Geol. Rundsch.*, *84*, 412–432.

European Space Agency (2004), Swarm—The Earth's magnetic field and environment explorers, *Tech. Rep. SP-1279(6)*, Paris. (Available at http://www.esa.int/esaLP/LPswarm.html)

Galdeano, A., V. Courtillot, and J.-L. Le Mouël (1980), La cartographie magnétique de la France au 1er juillet 1978, *Ann. Geophys.*, *36*(1), 85–106.

Haines, G. V. (1985), Magsat vertical field anomalies above 40°N from spherical cap harmonic analysis, *J. Geophys. Res.*, *90*(B3), 2593–2598.

Langel, R. A., and W. J. Hinze (1998), *The Magnetic Field of the Earth's Lithosphere*, Cambridge Univ. Press, New York.

Le Mouël, J. L. (1969), Sur la distribution des éléments magnétiques en France, Ph.D. thesis, Univ. de Paris, Paris.

Mandea, M. (2001), Observations magnétiques—Réseau magnétique de répétition, *Tech. Rep. 19*, Bur. Cent. de Magnet. Terr., Paris.

Manoj, C., A. Kuvshinov, S. Maus, and H. Lühr (2006), Ocean circulation generated magnetic signals, *Earth Planets Space*, *56*, in press.

Maus, S., H. Lühr, G. Balasis, M. Rother, and M. Mandea (2005), Introducing POMME, POtsdam Magnetic Model of the Earth, in *Earth Observation With Champ: Results From Three Years in Orbit*, edited by C. Reigber et al., pp. 293–298, Springer, New York.

Maus, S., M. Rother, K. Hemant, C. Stolle, H. Lühr, A. Kuvshinov, and N. Olsen (2006), Earth's lithospheric magnetic field determined to spherical harmonic degree 90 from CHAMP satellite measurements, *Geophys. J. Int.*, *164*(2), 319–330, doi:10.1111/j.1365-246X.2005.02833.x.

Pham, V. N., D. Boyer, and J.-L. Le Mouël (2000), Nouveaux arguments sur L'origine de L'anomalie Magnétique du bassin Parisien (AMBP) d'après les propriétés électriques de la croûte, *C.R. Acad. Sci.*, *331*, 443–449.

Ravat, D., K. A. Whaler, M. Pilkington, T. Sabaka, and M. Purucker (2002), Compatibility of high-altitude and satellite-altitude magnetic anomalies over Canada, *Geophysics*, *67*, 546–554.

Sabaka, T. J., N. Olsen, and M. Purucker (2004), Extending comprehensive models of the Earth's magnetic field with Ørsted and CHAMP data, *Geophys. J. Int.*, *159*, 521–547.

Thébault, E., J.-J. Schott, M. Mandea, and J.-P. Hoffbeck (2004), A new proposal for spherical cap harmonic modeling, *Geophys. J. Int.*, *159*, 83–103.

Thébault, E., J. J. Schott, and M. Mandea (2006), Revised spherical cap harmonic analysis (R-SCHA): Validation and properties, *J. Geophys. Res.*, *111*, B01102, doi:10.1029/2005JB003836.

Truffert, C., C. Gumiaux, J. Chantraine, J. Perrin, A. Galdeano, D. Gapais, M. Ballevre, F. Asfirane, P. Guennoc, and J.-P. Brun (2001), Levé géophysique aéroporté dans le Sud-Est du massif armoricain (Programme GéoFrance3D Armor2): Magnétisme et radiométrie spectrale, *C.R. Acad. Sci.*, *333*, 263–270.

Tyler, R., S. Maus, and H. Lühr (2003), Satellite observations of magnetic fields due to ocean tidal flow, *Science*, *299*, 239–240.

Wonik, T., A. Galdéano, A. Hahn, and P. Mouge (1992), Magnetic anomalies, in *A Continent Revealed: The European Geotraverse*, edited by D. Blundell, R. Freeman, and St Mueller, pp. 31–34, Cambridge Univ. Press, New York.

M. Mandea and E. Thébault, GeoForschungsZentrum Potsdam, Telegrafenberg, D-14473 Potsdam, Germany. (mioara@gfz-potsdam.de; erwan@gfz-potsdam.de)

J. J. Schott, Ecole et Observatoire des Sciences de La Terre, F-67000 Strasbourg, France. (jeanjacques.schott@eost.u-strasbg.fr)